

# **A comparative study of layer heating and continuous heating methods on prediction accuracy of residual stresses in selective laser melted tube samples**

Hui Huang <sup>a</sup>, Yiyu Wang<sup>a</sup>, Jian Chen <sup>a</sup>, Zhili Feng <sup>a\*</sup>

<sup>a</sup>Materials Science and Technology Division, Oak Ridge National Laboratory, 1 Bethel Valley Road, Oak Ridge, TN 37831, USA

\*Corresponding author

Tel.: 865-576-3797

E-mail address: [fengz@ornl.gov](mailto:fengz@ornl.gov)

## **Notice of Copyright**

This manuscript has been authored by UT-Battelle, LLC, under contract DE-AC05-00OR22725 with the US Department of Energy (DOE). The US government retains and the publisher, by accepting the article for publication, acknowledges that the US government retains a nonexclusive, paid-up, irrevocable, worldwide license to publish or reproduce the published form of this manuscript, or allow others to do so, for US government purposes. DOE will provide public access to these results of federally sponsored research in accordance with the DOE Public Access Plan (<http://energy.gov/downloads/doe-public-access-plan>).

## **Highlights:**

- (1) Simulation at layer-track level SLM is enabled by GPU accelerated explicit FEA.
- (2) Temperature field of each layer is simply referenced to top layer by node offsetting in a swept mesh.
- (3) Layer heating method provides reasonable prediction at significantly lower cost than continuous heating.
- (4) The modeling accuracy of residual elastic strain was validated by X-ray diffraction.

## Abstract

Thermal distortion and residual stresses are two important factors that affect the quality and reliability of steel parts manufactured by laser powder bed fusion (LPBF) processes. A cost-effective model for evaluation of those heat effects are needed to refine the manufacturing process and provide insights into the product design and heat treatment. In this study, the layer heating method and sophisticated track-layer scanning method were applied to simulate the thermo-mechanical response of IN625 tube parts built by LPBF. Based on the similarity of temperature field in each layer deposit, a swept mesh was constructed to perform the thermal analysis for top layer, with the rest of layers referring to the temperature by node number offsetting. A novel explicit finite element analysis (FEA) code accelerated by Graphics Processing Unit (GPU) was used for the massive-element numerical analysis. The computational accuracy and efficiency of the layer heating and track-layer scanning methods were compared in detail. It is shown that layer heating method can efficiently capture the pattern of stress distribution with reasonable accuracy in stress magnitude. The grouped track-layer scanning method can predict the residual stress and strain more accurately at a higher cost (5~10×). The elastic strain distribution was compared with the measurement by X-ray diffraction, confirming the accuracy of residual stress prediction.

**Keywords:** Laser powder bed fusion; Residual stress; FEA; X-ray diffraction; GPU

## 1. Introduction

Laser powder bed fusion (LPBF) or selective laser melting (SLM) has been increasingly employed to manufacture complex-shaped metallic parts layer by layer. The products usually exhibit reasonably good surface finish, mechanical properties, and design flexibility [1]. To date, experimental studies have advanced the fundamental understanding of powder interactions, fluid flow in the molten pool, and defects formation such as porosity and spattering [2]-[5]. At part scale, transient distortion and thermal stresses can pose risks of build failures due to buckling and cracking [6][7][8]. To extend service lives of the SLMed parts especially those under harsh environment such as high thermal load and pressure, residual stresses should be minimized by proactive processing and post-build heat or mechanical treatment. On the other hand, the cost of LPBF for large-scale components can be very high at early stage studies which may need trial-and-error procedures to figure out an optimum manufacturing plan. To accelerate the development cycle, high-fidelity numerical modeling along with state-of-art experiment characterization techniques can be utilized to predict the in-situ part distortion and residual stresses as a cost-effective tool to assist process optimization.

Due to the nature of LPBF, coupled multi-physics such as laser/powder interaction, thermal conduction, powder dynamics, heat and mass flow, and solidification need to be covered to construct a comprehensive model as described by Wei et. al [9]. Nevertheless, such high-resolution simulation of component-level LPBF is not realistic using the current computational power of ordinary computers or workstations. The challenges are governed by the size of powder and laser beam (tens of microns) and associated time scales (microseconds), in comparison to the part scale at ten to hundred millimeters and printing time at minutes to hours. Thus, millions of degrees of freedom and time steps are needed to define a complete thermo-mechanical model. Most studies deal with heat flow and transient stress/distortion in miniature coupons with a few laser scanning. Matsumoto et al. [10] analyzed the single layer SLM using a 2D plane stress model considering temperature dependence of material properties. The powder bed and the molten area were assumed to be continuous and both with very small stiffness and strength. Ahmed Hussein et al. [11] took advantage of ANSYS software suite to model the transient temperature and stress in strip coupon by single-layer laser scanning. It was found that the length of molten pool increases with the laser scanning speed, while the width and depth of the molten pool decreases. Promopatum and Yao [12] studied the effect of scanning length and energy input on residual stress in Ti-6Al-4V additive manufacturing. The computational domain in 2.5 mm cube with 20 scanning tracks are explored. The solution domain will be further limited if multi-physics such as powder dynamics and fluid flow are calculated. Lee and Zhang [13] developed a hybrid powder packing and heat/fluid flow model to solve transient temperature of two-track LPBF in a 1.0 mm  $\times$  0.4 mm region. Chen and Yan [14] conducted thermo-fluid and mechanical analysis of 2-layer 2-track electron beam melting process within a 2.14  $\times$  0.575  $\times$  0.185 mm<sup>3</sup> domain, which consumed over 1000 h for the coupled analysis. Feng and Ma et al. [15] developed a hybrid Newton–Raphson method and implicit method to reduce the computational time by more than 75% compared with commercial software Abaqus.

As a leading method to predict welding distortion in large structures, inherent strain method [16] and its variations (eigen strain, plasticity mapping, etc.) have been developed to reduce computational cost of component-scale LPBF. Dunbar et al. [17] analyzed the mechanical behavior of a cylindrical wall by LPBF using a code by Project Pan. The displacement profiles along the wall height were measured and a reasonable agreement between simulations and experimental measurements was obtained. Chen et al. [18] investigated the part distortion in direct laser sintering by a multiscale approach combining a microscale model to predict inherent strain and a macroscale model to predict distortion. However, residual stresses prediction by inherent strain method may overestimate the local stress distribution since an elastic analysis is used for part-scale computation. As a balance between time and accuracy, lumped layers or peak temperature approach can be applied to save considerable computational

cost. Prabhakar et al. [19] applied stationary heat flux to specified layers over a time period in the numerical model. Yang et al. [20] compared the line heating and layer heating model in modeling of thermal distortion of LPBF parts. The layer heating method is found to be promising in thermo-mechanical simulation. Xie et al. [21] and Ding et al. [22] aimed at the steady-state temperature distribution to reduce the computational time in simulation of direct energy deposition. The part distortions were predicted with high accuracy, but the residual stresses could be overestimated in wire and arc AM. Further investigation on cost-effective simulation approaches are needed.

In the framework of transient thermo-mechanical FEA, computational cost can be reduced by adaptive mesh refinement [23][24] and iterative substructure method [25] without compromising solution accuracy. For the first step of stress analysis, adaptive mesh and dual-mesh methods [26] can be employed to get the temperature history. Luo and Zhao [27] employed a mesh refining and coarsening scheme to accelerate the finite element analysis of temperature field. By optimizing multi-processor parallelization, layer level powder bed selective melting can be simulated 12~18 times faster than those by simulation without adaptive remeshing methods. The authors [24] have developed a dynamic mesh refining method to accelerate both the thermal and mechanical analyses. A speedup factor of 9 was achieved in modeling of wire and arc additive manufacturing, compared with the commercial software Abaqus. Recent developments have been made to use explicit FEM as the stress analysis solver and accelerate the computation based on GPU techniques [28] [29] [30]. An in-house explicit FEM code [31][32] based on GPU acceleration was employed to model the residual stress and strain distribution in two thin-wall LPBF builds.

In the present study, the residual stress and strain in tubes fabricated by LPBF was investigated by numerical modeling. The scanning pattern rotated every layer was considered, the grouping of track and layer approach [31] was employed to accelerate the thermo-mechanical analysis. A method of temperature mapping based on incremental node numbering through layers was developed to greatly reduce the computational effort in thermal analysis. Two different approaches namely layer heating method and track-layer continuous scanning method were utilized to analyze the stress distribution induced by LPBF. The computational accuracy and efficiency of the two approaches were compared and analyzed, providing useful guideline for such computation-intensive numerical studies. The numerical model was validated by X-ray diffraction measurement of residual elastic strain; therefore it will provide insight into residual stress and plastic strain distribution in additive manufactured parts.

## **2. Experimental study**

### **2.1 IN625 tube builds**

The study is part of the competition program “Additive Manufacturing (AM) Modeling Challenge Series: Macroscale Process-to-Structure” sponsored by Air Force Research Laboratory (AFRL). The experiment procedure, measurement and description are briefed here, more details can be found in the references [33] [34] [35]. For model validation, several IN625 tube builds with different inner diameters were fabricated by LPBF process using an EOS M280 metal 3D printer. The material for the builds was gas atomized IN625 powder, with particle size between 6~60  $\mu\text{m}$  in a bimodal distribution. A steel substrate (250 mm  $\times$  250 mm  $\times$  30 mm) was employed, and the preheat temperature was around 80  $^{\circ}\text{C}$ . The nominal processing parameters included laser spot diameter 0.1 mm, laser power 300 W, scanning speed 1230 mm/s, hatch spacing 100  $\mu\text{m}$ , and layer thickness 40  $\mu\text{m}$ . The laser scanning followed the rastering path with the stripe length of 10 mm. The scanning vector was rotated 67 $^{\circ}$  after completion of each layer. Two tube builds A67 and A68 were selected for numerical simulation and compared with experimental measurements. The dimensions of the designed geometries are illustrated in **Fig. 1**, the tubes both have an outer diameter of 20 mm and height of 25 mm. The wall thickness of Build A67 is 1 mm and that of A68 is 3 mm. Actual build height was 24.9 mm and outer diameter was about 19.86 mm for both tubes. The yield strength and tensile strength of the IN625 builds in different build orientations and temperature levels were tested by General Electric (GE) Global Research Center sponsored by AFRL [36], and defined in the thermo-mechanical analysis.

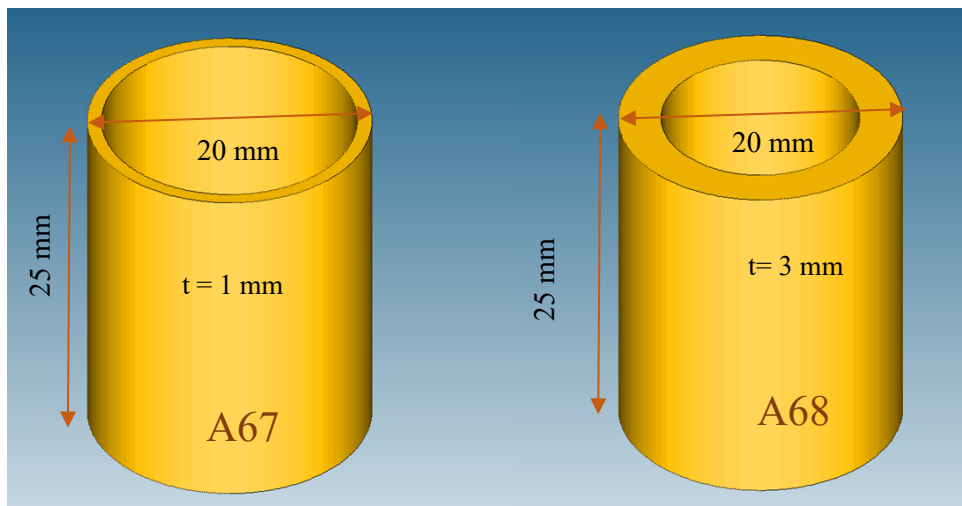


**Fig. 1** Dimensions of two tubes built by laser powder bed fusion

## 2.2 Measured elastic strain map by X-ray diffraction

After LPBF, the tube parts along with the attached section of base plate (roughly 30mm  $\times$  30 mm) were cut out using electric discharge machining for residual stress measurement. No post build heat treatment was applied to the builds after deposition. For direct validation of model

accuracy, residual elastic strains within the two IN625 tube builds were measured non-destructively. The strain component in radial direction ( $e_{rr}$ ) and vertical strain ( $e_{zz}$ ) in the tubes were measured by the Energy Dispersive Diffraction (EDD) technique using X-ray synchrotron at the Advanced Photon Source of Argonne National Laboratory [34]. The synchrotron beam used for diffraction was 0.05 mm in depth and 0.2 mm in height. The estimated full width at half maximum values for interaction depth for strain measurements are 2.7 mm and 4.6 mm for the radial component and vertical component, respectively. The horizontal diffraction angle  $2\theta_h$  was 4.5-4.75° for all EDD measurements. A schematic of the measurement setup is shown in **Fig. 2**. The incident beam was alligned with the hoop direction of the tube. The grains that fulfill Bragg condition within the interaction volume were counted and the strain of the grain set was averaged. The EDD measurement can provide strain resolution accuracy around 1e-4. More details of the EDD experiements can be found on the website [35]. **Figure 3** shows the elastic strain distribution on a cross section of tube A67. It is noted that horizontal coordinate is scaled by 4 times for better result visualization.

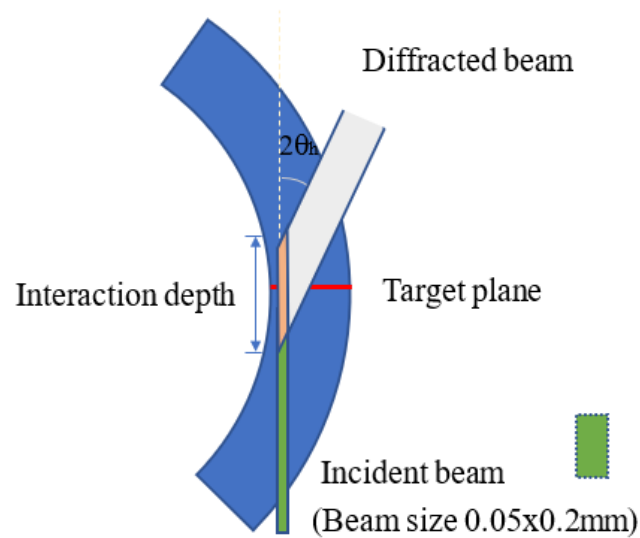


**Fig. 2** Schematic drawing of EDD measurement setup

### 3. Finite element model

In a previous study [31], an efficient numerical model with a moving heat source continuously heating on grouped tracks has been developed for thermo-mechanical analysis of LPBF. Several adjacent tracks across different layers are grouped and heated together, so that mesh size can be increased, and the total scanning time can be reduced. To further increase the computational efficiency, the layer heating method is investigated in the present study, with comparison to the track-layer continuous heating method. The two methods follow the same sequentially coupled thermo-mechanical analysis which is widely adopted to model residual stress and distortion in welding and additive manufacturing [22][37][38]. For the layer heating

method, three adjacent layers are simultaneously heated to melting temperature, and then naturally cooled down to room temperature.

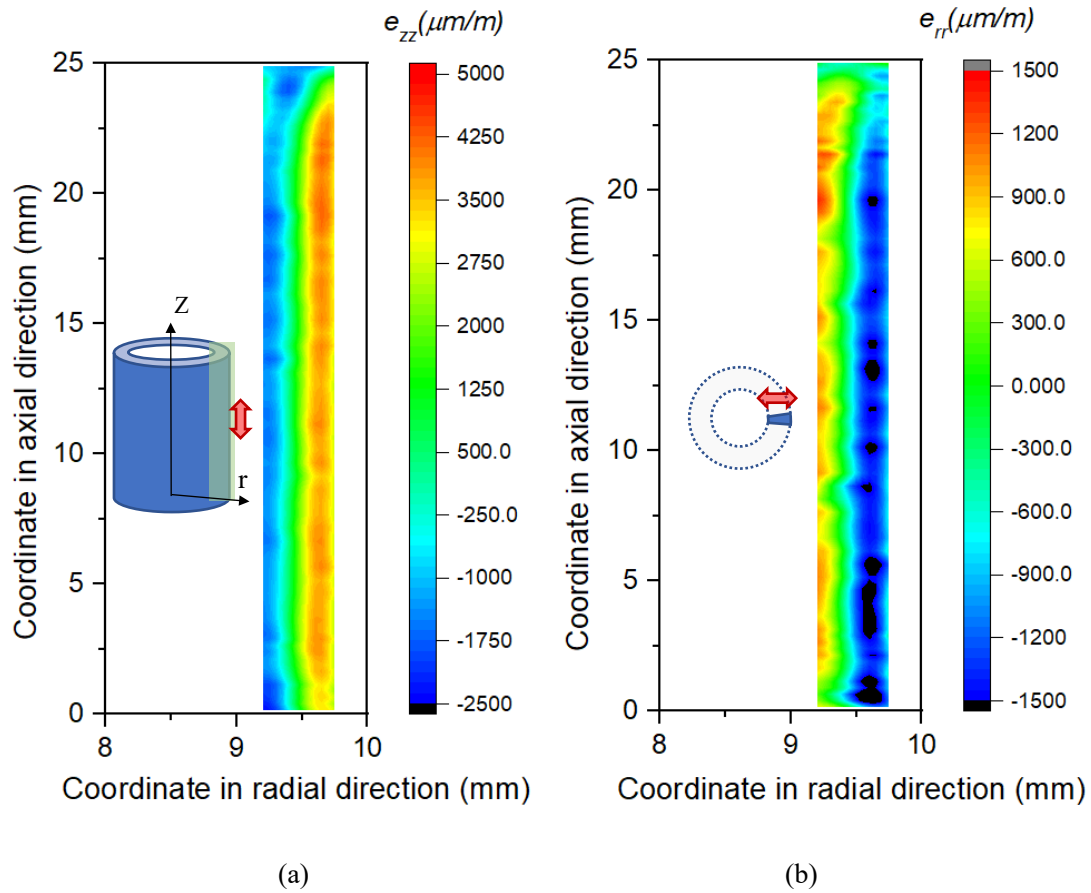
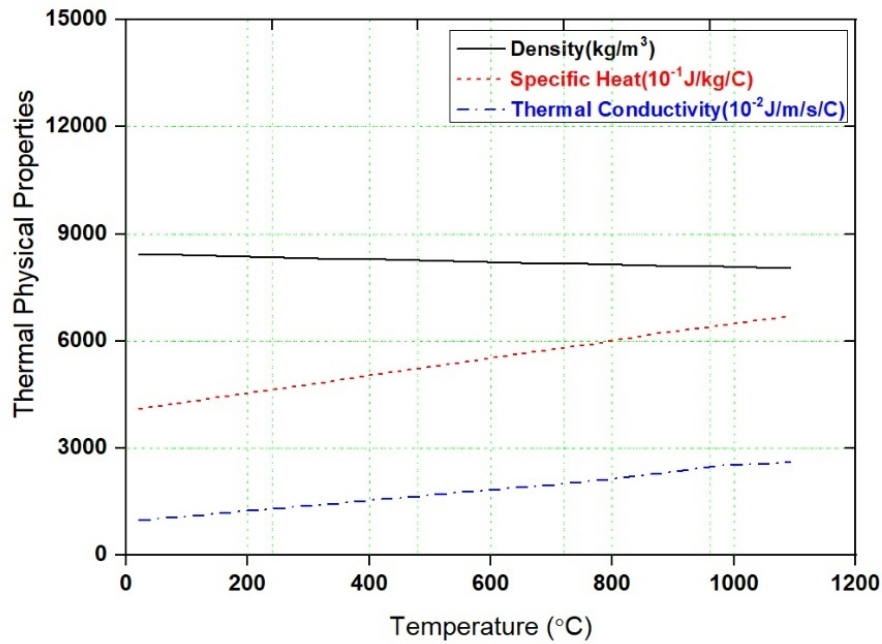


**Fig. 3** Elastic strain measurement by X-ray diffraction [34][35]: (a) elastic strain component in vorticle (axial) direction; (b) elastic strain component in radial direction.

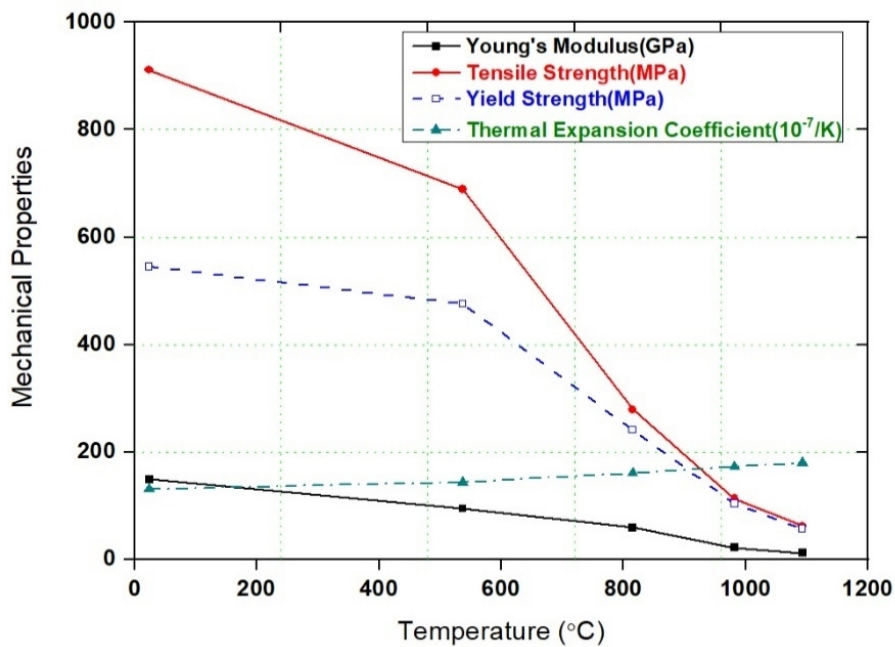
### 3.1 Thermal conduction analysis

Transient thermal analysis requires updating free surface definition and element heat capacity matrix as well as following laser scanning path of each layer, which can be time consuming. Taking tube model A67 as an example, the element size near the outer surface is about 0.15 mm and the total number of elements is 462,924. The heat conduction analysis of a single layer costs more than one hour using the implicit FEM with 8-core parallel computing. The estimated computational time for all 167 grouped layers would take 7 days. The uniform cross-section feature of the tubes and thermal field similarity in scanning pattern rotating can be taken advantage to generate the temperature history. An implicit solver JWRIAN developed by the Joining and Welding Research Institute [38] was used, which has high parallelizing performance on multi-core CPU using sparse matrix solver PARDISO. The thermal-physical properties of IN625 are shown in Fig. 4(a). Equivalent heat transfer is applied to all surfaces of the build to simulate the thermal conductance of powder bed. In an early study [39], a meso-scale model was developed to derive the equivalent conductivity as a function of particle

contact and temperature. Here, the equivalent heat transfer coefficient was further calibrated from minimum contact (0.28%) of powder using a single-track model. The values of heat transfer coefficient as function of temperature are listed in Table 1.



(a)



(b)

**Fig. 4** Temperature dependent material properties of IN625 material: (a) Thermal properties (b) Mechanical properties

Table 1 Equivalent heat transfer coefficient for IN625 LPBF build

Temperature (°C)	0	200	400	600	800	1000	1200
Heat transfer coeff. (W/°C/m <sup>2</sup> )	50	100	200	300	1000	2000	6000

In the simulation of layer heating, uniform heat flux is applied to a layer until the temperature reaches the melting point. To mimic the similar cooling rate in single-layer heating, an artificially increased heat transfer coefficient (three times larger) was employed. **Figure 5** shows the temperature distribution before cooling, indicating large thermal gradient in the layer thickness direction. In this finite element model, the nodes in the mesh are numbered linearly increases with the layer. With reference to top layer, the temperature history of the rest layers can be easily calculated by offsetting the node number in vertical direction. Since the whole layer is heated at the same time, no scanning pattern need to be modeled. For this type of layer heating method, only one analysis step is needed using the swept mesh and node numbering technique.

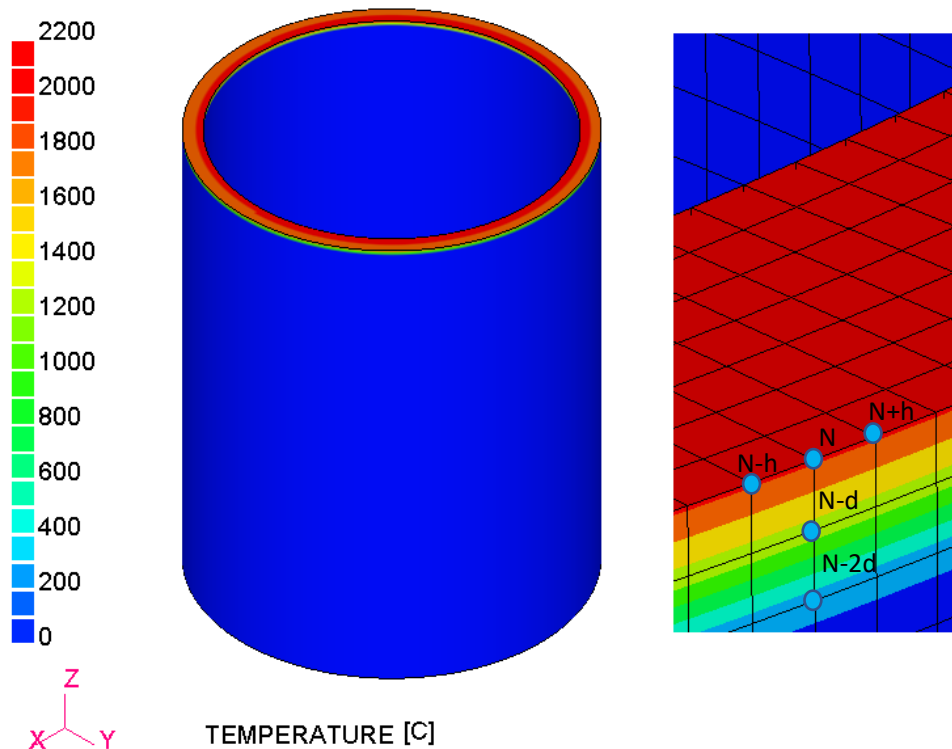


**Fig. 5** Temperature distribution in tube A67 predicted by layer heating method and node numbering pattern in thickness and hoop direction

In the case of thermal conduction analysis with a moving heating source, the detailed processing condition (scanning speed, laser spot diameter, hatching spacing etc.) should be

defined. The scanning path is rotated  $67^\circ$  around the axis of tube after depositing each layer. By using the grouping technique, the equivalent hatch spacing becomes 0.3 mm. To reduce the high computational cost for all layers, thermal analysis for the top layer with vertical scanning paths is calculated and then temperature of each layer printing is mapped from the baseline analysis by offsetting the node number in vertical direction and around the tube axis. For the moving laser scanning, Goldak double ellipsoidal heat source [40] was employed for the thermal conduction analysis. The heat flux  $q_f$  and  $q_r$  for the front and rear ellipsoid quadrants are described in **Eq. (1)** and **Eq. (2)**, respectively.

$$q_f = \frac{6\sqrt{3}F_f\eta Q_t}{a_f b c \pi \sqrt{\pi}} e^{-3(x-x_0)^2/a_f^2} e^{-3(y-y_0)^2/b^2} e^{-3(z-z_0)^2/c^2} \quad (1)$$

$$q_r = \frac{6\sqrt{3}F_r\eta Q_t}{a_r b c \pi \sqrt{\pi}} e^{-3(x-x_0)^2/a_r^2} e^{-3(y-y_0)^2/b^2} e^{-3(z-z_0)^2/c^2} \quad (2)$$

Where,  $Q_t$  denotes the total heat power, which is calculated from the grouped laser heat input  $Q_t = \xi G_T G_L Q$ .  $Q$  is the nominal power of single laser heat source.  $G_T$  and  $G_L$  are grouping factor of track and layer respectively. In this study, the two factors are assigned as 3.  $\xi$  is the interaction factor applied to total heat input combined from adjacent tracks and layers. A value 0.8 was assigned to  $\xi$ .  $\eta$  is the laser absorptivity which takes a value of 0.42 [31].  $F_f$  and  $F_r$  are factors for heat distribution to front and rear ellipsoids, and  $F_f + F_r = 2$  holds for conservation of heat input.  $x, y, z$  are coordinates for a point where the heat flux is evaluated.  $x_0, y_0, z_0$  are coordinates of the heat source center at the current time. The parameters  $a_f, a_r, b, c$  denote the semi-axes of the front ellipsoid and rear ellipsoid in welding direction.  $b$  and  $c$  are the semi-axes of the two ellipsoids in transverse direction and layer thickness direction, respectively. Here,  $a_f$  takes a value of 0.5 mm and  $a_r$  takes 0.8 mm,  $b$  and  $c$  both equal to 0.3 mm.

**Figure 6** shows the temperature distribution during LPBF by the moving heat source. Due to the grouping effect, the molten pool is obviously larger than single track-layer case which has a molten pool length at about 0.73 mm [31]. The peak temperature is about 2800 °C, which is below the boiling temperature. Such deviation from expectations proven experimentally can be attributed to the enlarged heat source model and limited space resolution (mesh size 0.2 mm) of the solid model. From the mechanical perspective, the melt pool size is more critical to the stress and strain development because the material properties such as Young's modulus and yield strength beyond the melting point is very small. The heating time for each layer is approximately 0.437s, and cooling time is 2 mins since multiple samples were fabricated on the powder bed at the same time.

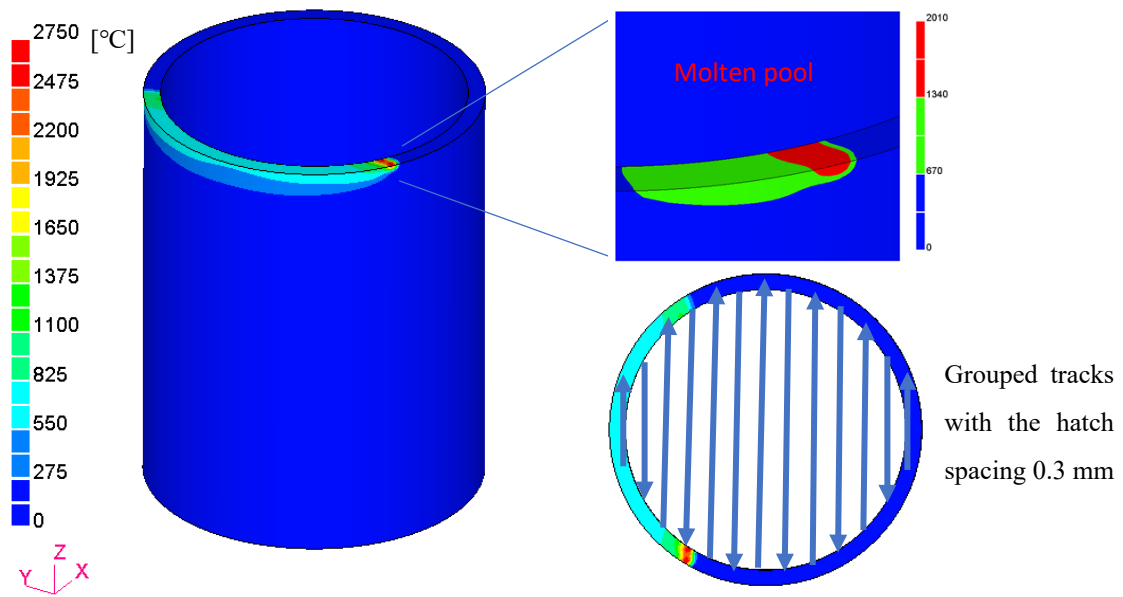


**Fig. 6** Temperature distribution predicted by track-layer method and schematic of laser scanning path of the baseline thermal analysis model

### 3.2 Mechanical analysis

The temperature history from thermal conduction analysis will be loaded on the mechanical model, which has the same mesh except for element type and boundary condition. The bottom of the tube is fixed at all three directions since the substrate plate is much stiffer due to large thickness. Element birth technique was implemented to model the additive manufacturing process, with elements activated if the average temperature from nodes is above 800 °C to stabilize the element distortion near melt pool. Before the element is heated up, the mechanical properties including Young's modulus and yield strength is assumed to have very small value (1% of original data). Due to the difference in mechanical properties in horizontal and vertical direction, the orthotropic plasticity hardening model [37] was employed in the simulation of transient stress behavior of tubes during LPBF. The same yield stresses are assumed in the horizontal plane, and the stress ratio between vertical yield stress and horizontal yield stress is 0.868 based on mechanical test results [31]. Young's modulus, thermal expansion coefficient and mechanical strengths were defined as functions of temperature as shown in **Fig. 4(b)** [31] [35].

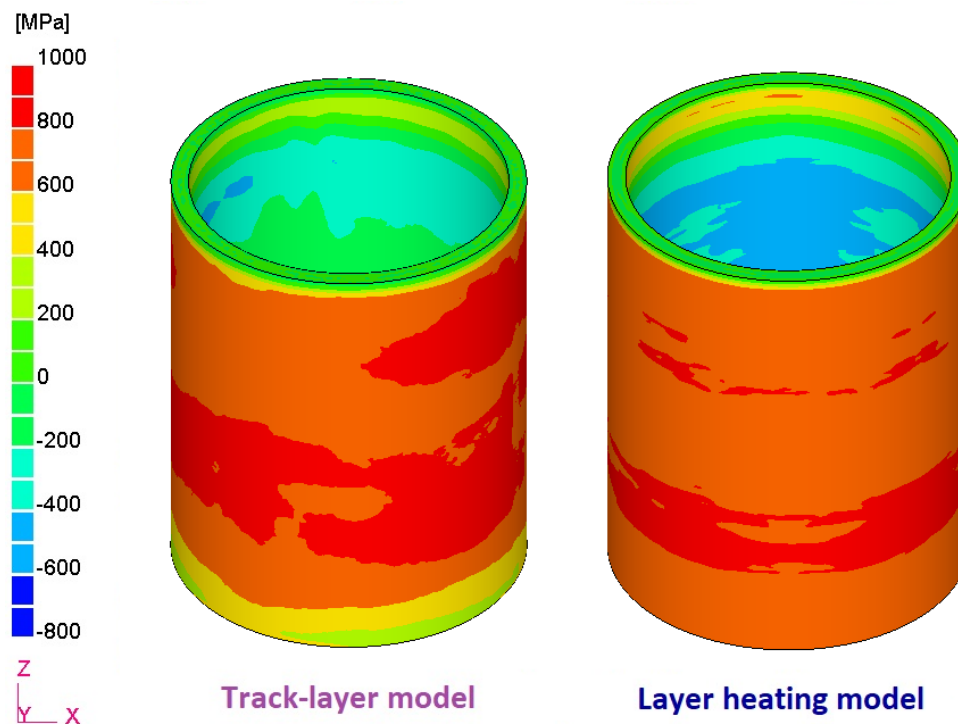
The stress analysis is carried out by a novel GPU-based explicit finite element code [24][30] [32] to save computational time. The code has proven high computing performance over commercial code such Abaqus by a factor more than 70 times in terms of wire and arc based additive manufacturing. The GPU can efficiently accelerate the computation of a numerical model which has tremendous number of elements such as in the case of LPBF. The computation platform is equipped with an Intel Xeon Silver 4110 Processor (8 Core, 2.1Ghz,

11M Cache) and a NVIDIA Tesla P100 (16GB, HBM2). Compared with conventional implicit FEM, the analysis by explicit FEM can achieve better parallelizing performance and consume much less system memory, which is beneficial for very large-scale models such as multi-layer additive manufacturing.

## 4. Results and discussion

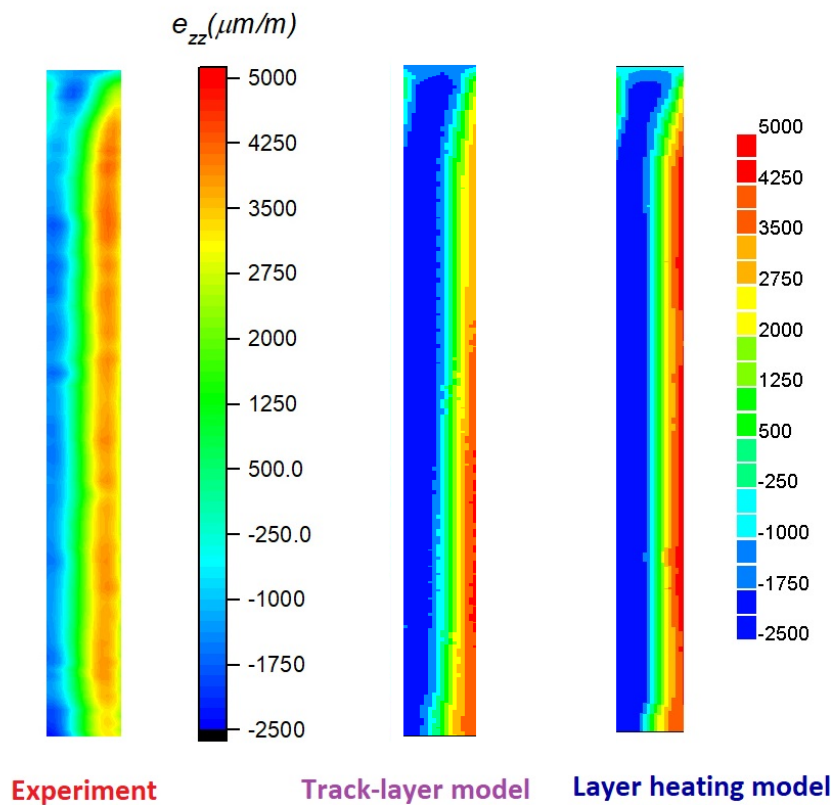
### 4.1 Residual stress and elastic strain in thin-wall tube

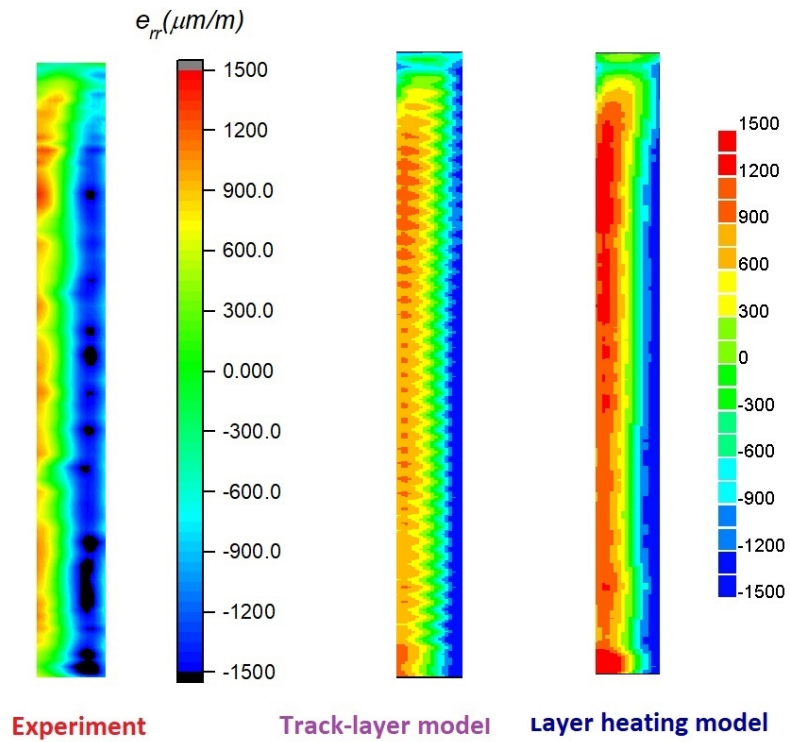
**Figure 7** shows the residual stresses calculated by the layer heating method and track-layer continuous heating method for tube A67. The axial (vertical) stress exhibits high tensile stress up to 850 MPa near the outer surface and relatively lower compressive stress (-500 MPa) near the inner surface because of stress balance. The two stress contours are overall similar, except that vertical stress at the bottom part of tube is higher in the case of layer heating model than that in track-layer model, which is probably caused by the simultaneous heating and cooling on a fixed plate. The stress contour is basically axisymmetric about the central line due to the cylindrical shape of build and rotating laser scanning pattern. It is also noted that, relatively high tensile stress (400~600 MPa) shows up near inner surface of top part of the tube. The radial stress (stress component along radial direction) as well as the hoop stress are much lower (<400 MPa) for this thin-walled tube, which will be discussed in comparison with those of larger tube A68.



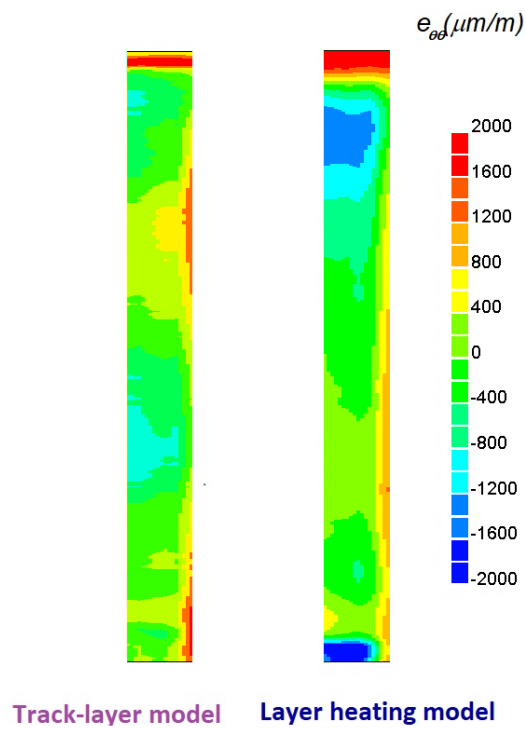
**Fig. 7** Vertical residual stress in 1-mm thick thin-wall tube A67 by layer heating method and track-layer scanning method

**Figure 8** shows the elastic strain results after the fabrication of A67 build, featuring significant variations through thickness for all strain components. Similar to axial stress distribution, the vertical strain  $e_{zz}$  (axial direction strain) shows a compressive-tensile pattern through wall thickness, indicating the vertical strain has a dominating effect on the stress distribution. The maximum strain near outer surface of thin wall is about 0.5% which grossly exceeds the elastic limit of IN625, hence high residual stresses is produced after LPBF. On the other hand, the peak values of radial elastic strain ( $e_{rr}$ ) and hoop elastic strain ( $e_{\theta\theta}$ ) as shown in **Fig. 8** (b)~(c) are much lower than the vertical strain. Therefore, strain in vertical direction is critical to the principle stress which is responsible for the failure of materials during build and service. This prediction result is also consistent with the experimental observation that the lower strength properties are obtained when the specimen is built along vertical direction (Z direction) [35].





(b)

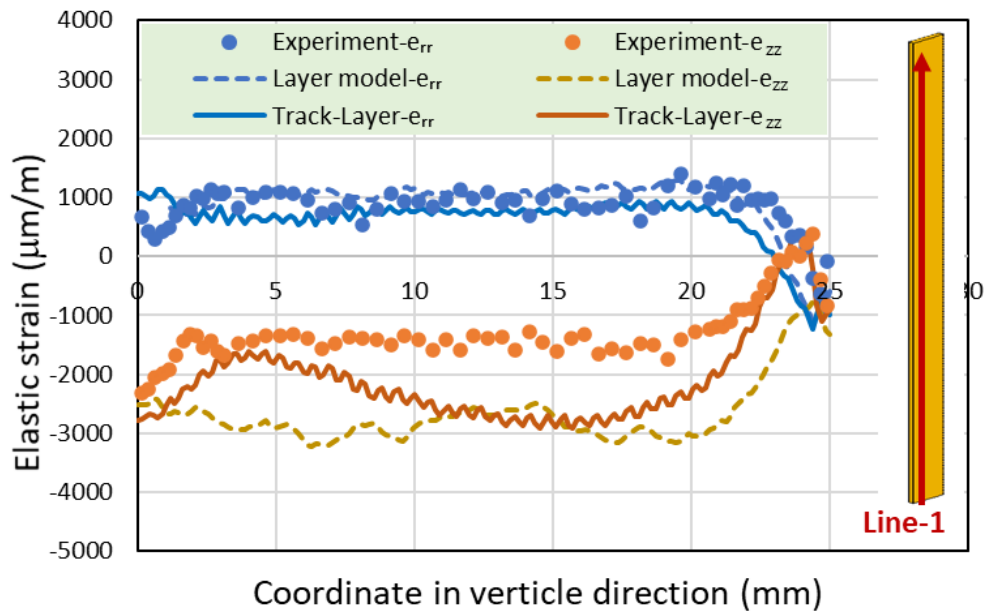


(c)

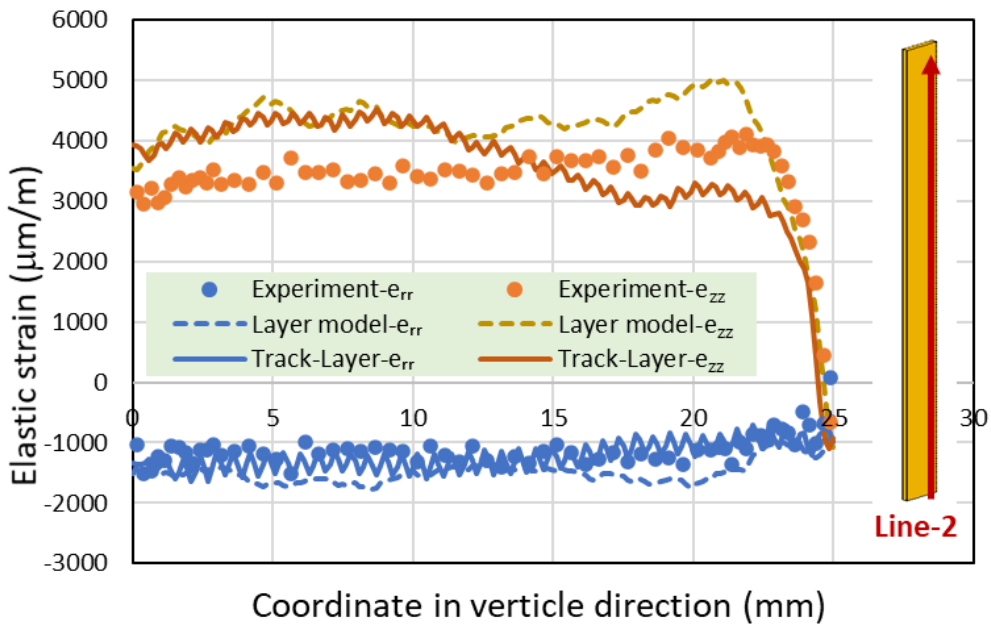
**Fig. 8** Elastic strain maps of printed tube (Model-A67): (a) vertical strain component; (b) radial strain component (c) hoop strain component (horizontal dimension scaled by 4 times)

**Figure 8** also compares the residual elastic strain predicted by the numerical model and those measured by X-ray synchrotron. Overall, the strain maps have a close correlation among each other in terms of distribution zone of tensile and compressive strains. The track-layer model has a better accuracy in capturing the strain magnitude on the inner wall which is a little overestimated by the layer heating method. This can be understood from the constraint viewpoint that materials in the whole layer are activated in the layer heating model, which causes a stiffer constraint for the strain development. Whereas, materials in layer and track model are progressively activated, better representing the constraint evolution during additive manufacturing process. Similarly, the model by layer heating predicted a wider region of tensile hoop strain on the top layer and compressive hoop strain near the bottom layer. For this tube geometry, no experiment measurement on hoop strain was available for comparison with model.

For more quantitative comparison, the strain profile along two lines (0.2 mm offset) near inner and outer surfaces are plotted in **Fig. 9**. In general, the two modeling approaches predict the pattern and magnitude of elastic strain with good confidence considering the complexity of the LPBF process and material property anisotropy. The radial strain ( $e_{rr}$ ) is smaller than vertical strain ( $e_{zz}$ ) especially on the outer surface, which is mainly controlled by the free stress condition on the tube surfaces. The radial strain is in a range between -0.15% and 0.15% through the thickness of tube build. Compared with experimental data, both models have a deviation of  $\pm 0.12\%$  in predicting the vertical elastic strain. From results along line 1, the averaged vertical strain by experiment is about -0.15%, while those predicted by layer heating model are nearly -0.3%. For vertical strain along line 2, the averaged value by experiment is about 0.35%, with reference to those ( $\sim 0.42\%$ ) by modeling with layer heating method. The experimental measurement is based on the interaction volume with a depth of several millimeter in hoop direction, whereas the modeling results are extracted from the cut plane through the tube axis. A single EDD measurement may cover grains with both tensile and compressive strain that can cause lower strain value compared with modeling result. It is noted that the interaction depth in radial strain measurement is 2.7 mm which is about half of that (4.6 mm) in vertical strain measurement. Thus, the comparison of radial strain between model and experiment is more trustworthy in validating the accuracy of the model. Overall, the discrepancy of radial strain measured by experiment and that predicted by model is small on both inner and outer surfaces of the A67 tube. On the other hand, the track-layer grouping can lead to lower resolution of residual stress and strain at regions where strain gradient is large in actual build. A higher prediction accuracy may be achieved by finer modeling of track and layer continuous heating at the cost of longer computational time, which is currently not suitable for component scale LPBF.



(a)



(b)

**Fig. 9** Comparison of strain profile between models and experimental measurements: (a) results along a line on the inner surface; (b) results along a line on the outer surface

#### 4.2 Residual stresses in thicker tube build

The two builds A67 and A68 with different inner diameters were simulated by the layer heating method as well as the track-layer continuous scanning method. The simulation results are

compared with the available X-ray synchrotron measurement data to investigate the effect of part dimension on residual stress distribution. The tube A68 has a larger wall thickness (3 mm) than tube A67 (1 mm), resulting in a larger constraint which is prone to generate higher residual stresses. The understanding of stress pattern is also helpful in guiding subsequent heat treatment and fatigue analysis for builds with different geometries and dimensions.

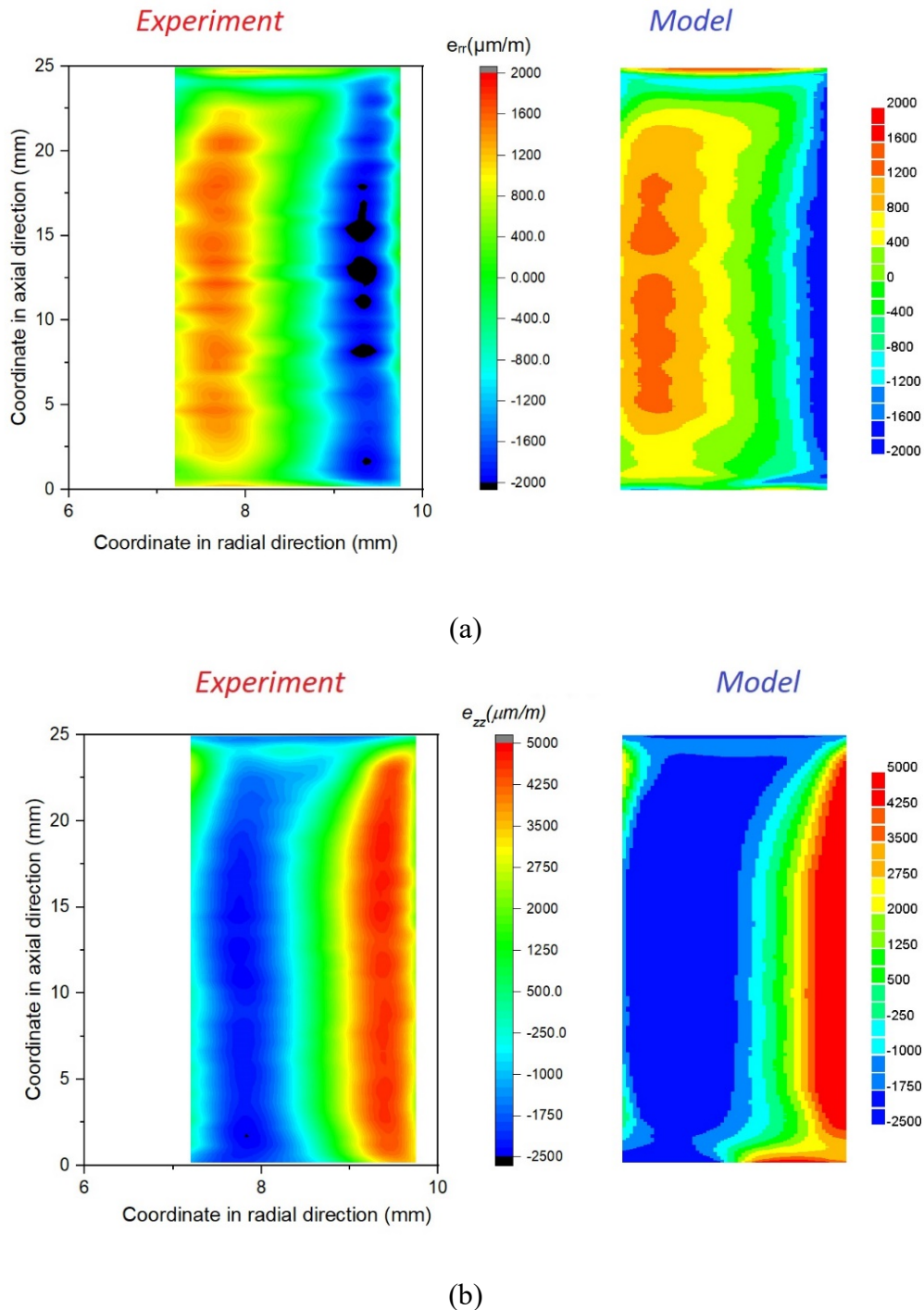


**Fig. 10** Elastic strain maps of tube build A68: (a) radial strain component; (b) vertical elastic strain (horizontal dimension scaled by 4 times)

The residual elastic strain of A68 tube is compared between model prediction and experiment measurement as shown in **Fig. 10**. Note that, the simulation results by layer heating was plotted here, the computational performance of the two simulation methods will be compared later. For this tube with larger wall thickness, the radial strains predicted by model and measured by X-ray both feature compressive strain on outer surface (right side of the strain map) and tensile strain on inner surface (left side of strain map) of the build, as shown in subfigure (a). Peak radial strain seems to appear in the region about 0.7 mm from inner surface, with a value about 0.15% close to that in thinner tube A67. The strain concentration on the top layer was also captured by the model. As shown in **Fig. 10(b)**, the vertical elastic strain again has a high tensile strain distribution near outer surface, which is on the opposite of that in radial strain. Limited by the free surface condition, the vertical strain near the top layer is basically uniform, with a compressive strain of only about -0.1%. Overall, the layer heating model well resembles the residual elastic strain distribution in experimental specimens, which provides indirect validation to the residual stress predictions.

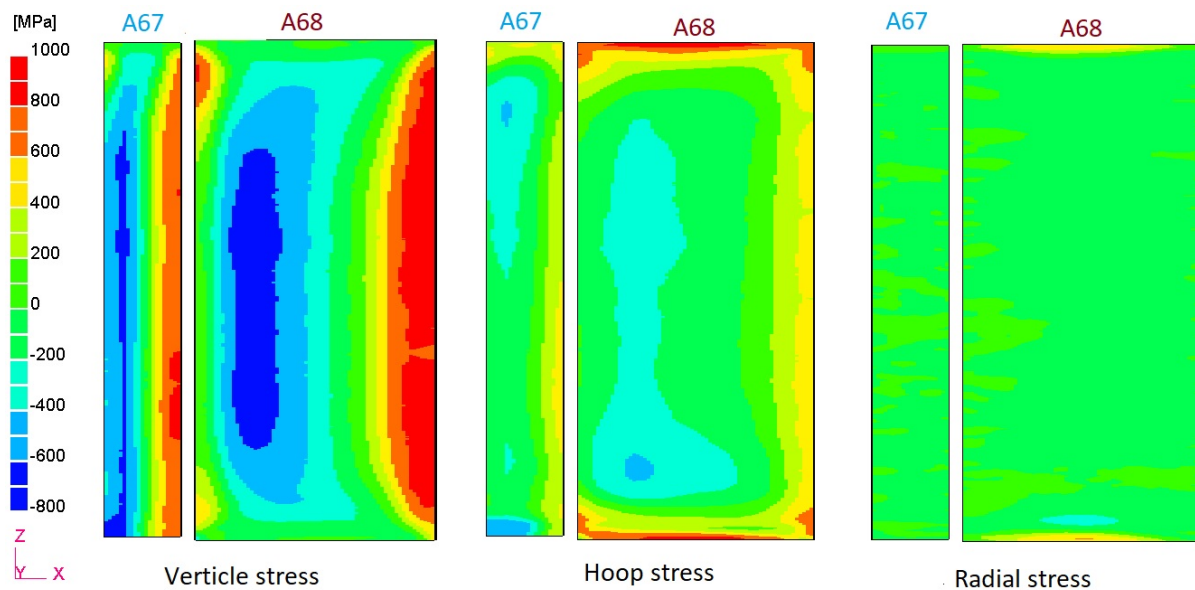


**Fig. 11** Comparison of residual stress distribution on tube cross-section

The residual stresses predicted by the numerical model are plotted in **Fig. 11** for the two printed tubes with different wall thicknesses. The vertical stress (or axial stress) shows compressive stress near inner surface while tensile stress near outer surface. The size of high stress region is wider in tube A68 which has a wall thickness three times larger than that of tube A67. The peak stress is almost 850 MPa which is slightly lower than the tensile strength 920 MPa at room temperature. Based on the stress distribution, heat treatment with non-uniform temperature can be applied to reduce the stress magnitude. In addition, shot peening or laser peening can also be employed to alter the stress distribution by introducing compressive stress

on the outer surface. In terms of hoop stress, stress concentration was only observed near the top and bottom layer, and the thicker tube exhibits much higher stress magnitude. After experiencing rapid heating and cooling, the material of top layer tends to shrink under restraint by existing build beneath the layer.

### 4.3 Computational cost by the two approaches

For A67 and A68 simulation models, the computational time is summarized in **Table 1**. In the case of layer heating method, both thermal analysis and mechanical simulation took less than three hours for the two models, which is affordable for product design. The primary reason for the short time is that significantly fewer number of time steps are involved in thermo-mechanical analysis. In the case of A67 simulation, the time steps for thermal analysis is 192, and the thermal analysis is only needed for top layer owing to the bottom-up mesh pattern and incremental node mapping. Accordingly, the time steps for mechanical analysis was  $167 \times 192 = 32,064$  which is a large number for conventional implicit FEM. With the GPU accelerated explicit FEM, the computational time for each time step can be greatly reduced. The time step in modeling of LPBF is usually very small ( $\sim 0.1$  ms) which is suitable for explicit FEM. One more advantage of explicit FEM over implicit FEM is that, the computational cost almost linearly increases with the number of elements other than in a quadratic way.

**Table 2** Computational cost (in hours) of thermo-mechanical simulation of SLM

Simulation method	Layer heating		Track-layer scanning	
	Thermal	Mechanical	Thermal	Mechanical
Tube A67	1.2	1.6	11.8	5.5
Tube A68	2.8	3.0	67.2	39.1

If track-layer continuous scanning is modeled, much longer time (5~10 $\times$ ) will be required due to grossly increased number of time steps. In the case of A67 model, the thermal analysis to simulate continuous scanning of each layer requires about 2400 time steps, more than ten times of that in layer heating model. The increase of time steps in large model A68 is even more significant ( $\sim 7500$  time steps). The mechanical analyses by developed in-house explicit FEM code are completed within a shorter time frame compared with thermal analysis. It is also found that, the variation of simulation cost by layer heating method is much less sensitive to the model

scale, while that by track-layer method dramatically increases by about 6 times when the model is about 3 times larger in wall thickness. Due to multi-million degrees of freedom (DOF) and thousands of time steps involved LPBF model, the thermo-mechanical simulation by conventional FEM would require weeks to months of computational time. This is even more challenging when models at different scales (fluid flow, heat transfer, mechanical models) are linked to provide high-fidelity prediction of microstructure, porosity, and residual stresses. Further reduction of computational time can be achieved with incorporation of adaptive mesh method as well as more advanced high-throughput GPU. Such efficient modeling tool will provide insight into process development and heat treatment plan to control the residual stresses in additively manufactured parts.

## **5. Concluding remarks**

Thermo-mechanical finite element analysis was employed to predict the residual stresses of tubes fabricated by selective laser melting. Two simulation approaches including the layer heating method and the track-layer continuous heating method were examined and compared with experimental measurements. The solution accuracy and the computational time were summarized to provide guidance for cost-effective analysis. The following conclusions can be drawn:

- (1) For tubes fabricated by selective laser melting, high tensile stress in axial direction will be produced on the outer surface while compressive stress will exist on the inner surface as a balance. Hoop stress and radial stress in overall region except for top and bottom part are much lower than axial stress.
- (2) With the increase of tube thickness, the size of region with high axial (vertical) stress increases proportionally. The magnitude of the radial stress and particularly the hoop stress on top and bottom layer also increases due to the larger constraint.
- (3) Simulation by layer heating method predict residual stress with a reasonable accuracy at much lower cost than that by track-layer continuous heating method. The advantage is even more remarkable if the part scale is larger because the time step is nearly constant for each layer.
- (4) The computational time of the simulation by the layer heating method is quite affordable for both thermal and mechanical analysis. In the framework of the track-layer model with a moving heat source, the thermal analysis appears to take considerable time, whereas mechanical analysis can be completed in a reasonable timeframe by GPU accelerated code.
- (5) The computational accuracies of the two solution techniques are validated by experimental characterization. The maps of elastic strain have a good correlation between the model prediction and the X-ray measurements, which confirms the validity of model in residual stress simulation.

## Acknowledgement

This research was sponsored by the US Department of Energy, Advanced Manufacturing Office, under a prime contract with Oak Ridge National Laboratory (ORNL). ORNL is managed by UT-Battelle, LLC for the U.S. Department of Energy under Contract DE-AC05-00OR22725.

## Conflict of Interest Statement

On behalf of all authors, the corresponding author states that there is no conflict of interest.

## References

- [1] Frazier, W. E. (2014). Metal additive manufacturing: a review. *Journal of Materials Engineering and performance*, 23(6): 1917-1928.
- [2] DebRoy T, Wei HL, Zuback JS, et al. (2018) Additive manufacturing of metallic components—process, structure and properties. *Progress in Materials Science*. 92:112-224.
- [3] du Plessis A, le Roux S G, Booysen G, et al. (2016) Directionality of cavities and porosity formation in powder-bed laser additive manufacturing of metal components investigated using X-ray tomography. *3D Printing and Additive Manufacturing*, 3(1): 48-55.
- [4] King W E, Anderson A T, Ferencz R M, et al. (2015) Laser powder bed fusion additive manufacturing of metals; physics, computational, and materials challenges. *Applied Physics Reviews*, 2(4): 041304.
- [5] Mukherjee T, Wei HL, De A and DebRoy T (2018) Heat and fluid flow in additive manufacturing—Part II: Powder bed fusion of stainless steel, and titanium, nickel and aluminum base alloys. *Computational Materials Science*, 150: 369-380.
- [6] Santos LS, Gupta SK, Bruck HA (2018). Simulation of buckling of internal features during selective laser sintering of metals. *Additive Manufacturing*, 23:235-245.
- [7] Kayacan MY, Özsoy K, Duman B, Yilmaz N and Kayacan MC (2019) A study on elimination of failures resulting from layering and internal stresses in Powder Bed Fusion (PBF) additive manufacturing. *Materials and Manufacturing Processes*, 34(13):1467-1475.
- [8] Tran HT, Chen Q, Mohan J, To AC (2020). A new method for predicting cracking at the interface between solid and lattice support during laser powder bed fusion additive manufacturing. *Additive Manufacturing*, 32: 101050.
- [9] Wei HL, Mukherjee T, Zhang W, Zuback JS, Knapp GL, De A, and DebRoy T (2020) Mechanistic models for additive manufacturing of metallic components. *Progress in Materials Science*, 100703.
- [10] Matsumoto M, Shiomi M, Osakada K, Abe F (2002) Finite element analysis of single

- layer forming on metallic powder bed in rapid prototyping by selective laser processing. *International Journal of Machine Tools and Manufacture*, 42(1): 61-67.
- [11] Hussein A, Hao L, Yan C, Everson R (2013) Finite element simulation of the temperature and stress fields in single layers built without-support in selective laser melting. *Materials & Design* (1980-2015), 52: 638-647.
- [12] Promopattum P, Yao SC (2020) Influence of scanning length and energy input on residual stress reduction in metal additive manufacturing: Numerical and experimental studies. *Journal of Manufacturing Processes*, 49: 247-259.
- [13] Lee YS, Zhang W (2016) Modeling of heat transfer, fluid flow and solidification microstructure of nickel-base superalloy fabricated by laser powder bed fusion. *Additive Manufacturing* 12: 178-188.
- [14] Chen F, Yan W (2020) High-fidelity modelling of thermal stress for additive manufacturing by linking thermal-fluid and mechanical models. *Materials & Design*, 196: 109185.
- [15] Feng Z, Ma N, Li W, Narasaki K, Lu F (2020). Efficient analysis of welding thermal conduction using the Newton–Raphson method, implicit method, and their combination. *The International Journal of Advanced Manufacturing Technology*, 111(7), 1929-1940.
- [16] Ueda Y, Murakawa H, Ma N (2012) *Welding deformation and residual stress prevention*. Elsevier, Butterworth-Heinemann. doi:10.1016/C2011-0-06199-9
- [17] Dunbar AJ, Denlinger ER, Gouge MF, Michaleris P (2016) Experimental validation of finite element modeling for laser powder bed fusion deformation, *Additive Manufacturing*, 12: 108-120
- [18] Chen Q, Liang X, Hayduke D, Liu J, Cheng L, Oskin J, Whitmore R, To AC. (2019) An inherent strain based multiscale modeling framework for simulating part-scale residual deformation for direct metal laser sintering. *Additive Manufacturing*. 28:406-18.
- [19] Prabhakar P, Sames WJ, Dehoff R, Babu SS. (2015) Computational modeling of residual stress formation during the electron beam melting process for Inconel 718. *Additive Manufacturing*. 7: 83-91.
- [20] Yang YP, Jamshidinia M, Boulware P, Kelly SM (2018) Prediction of microstructure, residual stress, and deformation in laser powder bed fusion process. *Computational Mechanics*, 61(5):599-615.
- [21] Xie R, Chen G, Zhao Y, et al. (2019) In-situ observation and numerical simulation on the transient strain and distortion prediction during additive manufacturing. *Journal of Manufacturing Processes*, 38: 494-501.
- [22] Ding J, Colegrove P, Mehnen J, Williams S, Wang F, Almeida PS (2014) A computationally efficient finite element model of wire and arc additive manufacture. *The International Journal of Advanced Manufacturing Technology*, 70(1-4): 227-236.
- [23] Denlinger ER, Gouge M, Irwin J, Michaleris P (2017) Thermomechanical model

- development and in situ experimental validation of the Laser Powder-Bed Fusion process. *Additive Manufacturing*, 16:73-80.
- [24] Huang H, Ma N, Chen J, Feng Z, Murakawa H (2020). Toward large-scale simulation of residual stress and distortion in wire and arc additive manufacturing. *Additive Manufacturing*, 101248.
- [25] Murakawa H, Ma N, Huang H (2015) Iterative substructure method employing concept of inherent strain for large-scale welding problems. *Weld World*. 59(1):53-63. doi:10.1007/s40194-014-0178-z.
- [26] Huang H, Ma N, Murakawa H, Feng Z (2019) A dual-mesh method for efficient thermal stress analysis of large-scale welded structures. *The International Journal of Advanced Manufacturing Technology*. 103(1-4):769-80.
- [27] Luo Z, Zhao Y (2020) Efficient thermal finite element modeling of selective laser melting of Inconel 718. *Computational Mechanics*, 65(3): 763-787.
- [28] Ikushima K, Shibahara M (2014) Prediction of residual stresses in multi-pass welded joint using Idealized Explicit FEM accelerated by a GPU. *Comput. Mat. Sci.* 93:62-67. doi:10.1016/j.commatsci.2014.06.024
- [29] Ma N (2016) An accelerated explicit method with GPU parallel computing for thermal stress and welding deformation of large structure models. *Int J Adv Manuf Tech.* 87 (5-8): 2195-2211. doi: 10.1007/s00170-016-8542-3
- [30] Huang H, Chen J, Carlson B, Wang H-P, Crooker P, Frederick G, Feng Z, Prediction of residual stresses in a multipass pipe weld by a novel 3D finite element approach. *American Society of Mechanical Engineers*. In ASME 2018 Pressure Vessels and Piping Conference (Paper No. PVP2018-85044, pp. V06BT06A084). doi:10.1115/pvp2018-85044.
- [31] Huang H, Wang Y, Chen J, Feng Z, Efficient numerical model for predicting residual stress and strain in parts manufactured by laser powder bed fusion, submitted to *Journal of Physics: Materials*, under review.
- [32] Huang H, Chen J, Feng Z, Wang H-P, Cai W, Carlson B (2021) Large-scale welding process simulation by GPU parallelized computing, *Welding Journal*, In press
- [33] Groeber M, Schwalbach E, Musinski W, Shade P, Donegan S, Uchic M, Sparkman D, Turner T, Miller J. (2018) A Preview of the US Air Force Research Laboratory Additive Manufacturing Modeling Challenge Series. *JOM*. 70(4):441-4.
- [34] Chuang AC, Park JS, Musinski JS, Shade PA, et al. (2020) Residual stresses formed in additively-manufactured Inconel 625 under a range of specimen configurations
- [35] <https://materials-data-facility.github.io/MID3AS-AM-Challenge/>
- [36] Project 4026: Development of Distortion Prediction and Compensation Methods for Metal Powder Bed Fusion Additive Manufacturing, Tech. Rep. America Makes Program sponsored by the Air Force Research Laboratory Under Agreement Number FA8650-12-2-7230 (2018)

- [37] Yang Y, Allen M, London T, Oancea V. (2019) Residual strain predictions for a powder bed fusion Inconel 625 single cantilever part. *Integrating Materials and Manufacturing Innovation* 8(3):294-304.
- [38] Huang H, Murakawa H (2015) Dynamic mesh refining and iterative substructure method for fillet welding thermo-mechanical analysis, *Comput. Model. Eng. Sci.* 106: 187–201.
- [39] Chen J, Zheng L, Feng Z, Zhang W, Dehoff RR (2013) Prediction of Material Thermal Properties and Beam-Particle Interaction at Meso-Scale during Electron Beam Additive Manufacturing. *Materials Science & Technology Conference*, Montreal, Canada
- [40] Goldak J, Chakravarti A, Bibby M (1984) A new finite element model for welding heat sources. *Metallurgical transactions B* 15(2): 299-305.

### Figure caption list

Fig. 1 Dimensions of two tubes built by laser powder bed fusion

Fig. 2 Schematic drawing of EDD measurement setup

Fig. 3 Elastic strain measurement by X-ray diffraction [34][35]: (a) elastic strain component in verticle (axial) direction; (b) elastic strain component in radial direction

Fig. 4 Temperature dependent material properties of IN625 material: (a) Thermal properties (b) Mechanical properties

Fig. 5 Temperature distribution in tube A67 predicted by layer heating method and node numbering

Fig. 6 Temperature distribution predicted by track-layer method and schematic of laser scanning path

Fig. 7 Vertical residual stress in 1-mm thick thin-wall tube A67 by layer heating method and track-layer scanning method

Fig. 8 Elastic strain maps of printed tube (Model-A67): (a) vertical strain component; (b) X-ray diffraction (c) hoop strain component (horizontal dimension scaled by 4 times)

Fig. 9 Comparison of strain profile between models and experimental measurements: (a) results along a line on the inner surface; (b) results along a line on the outer surface

Fig. 10 Elastic strain maps of tube build A68: (a) radial strain component; (b) vertical elastic strain

Fig. 11 Comparison of residual stress distribution on tube cross-section

**Table caption list**

**Table 1** Equivalent heat transfer coefficient for IN625 LPBF build

**Table 2** Computational cost (in hours) of thermo-mechanical simulation of SLM